Incommensurate spin density wave and magnetocaloric effect in the metallic triangular lattice $HoAl_2Ge_2$

Fei Gao,[1,2] Jieming Sheng,[3,4,*] Weijun Ren,[1,2,†] Qiang Zhang,[5] Xiaohua Luo,[6] Ji Qi,[1,2] Mengru Cong,[1,2] Bing Li,[1,2] Liusuo Wu,[4,7] and Zhidong Zhang[1,2]

[1]*Shenyang National Laboratory for Materials Science, Institute of Metal Research, Chinese Academy of Sciences, 72 Wenhua Road, Shenyang 110016, China*

[2]*School of Materials Science and Engineering, University of Science and Technology of China, Shenyang 110016, China*

[3]*Academy for Advanced Interdisciplinary Studies, Southern University of Science and Technology, Shenzhen 518055, China*

[4]*Department of Physics, Southern University of Science and Technology, Shenzhen 518055, China*

[5]*Neutron Science Division, Oak Ridge National Laboratory, Oak Ridge, Tennessee 37831, USA*

[6]*Jiangxi Key Laboratory for Rare Earth Magnetic Materials and Devices, College of Rare Earths, Jiangxi University of Science and Technology, Ganzhou 341000, China*

[7]*Shenzhen Key Laboratory of Advanced Quantum Functional Materials and Devices, Southern University of Science and Technology, Shenzhen 518055, China*

(Received 7 May 2022; accepted 11 October 2022; published 21 October 2022)

We report the magnetic structure and the magnetocaloric effect (MCE) of the ternary compound $HoAl_2Ge_2$ with a trigonal $CaAl_2Si_2$-type crystal structure. A neutron powder diffraction experiment reveals that $HoAl_2Ge_2$ exhibits an incommensurate spin density wave (SDW) with a propagation vector $\boldsymbol{k} = (0.23,\ 0,\ 0.06)$. The special arrangement of magnetic moments in $HoAl_2Ge_2$ induces interesting physical phenomena and large magnetocaloric effects. The rise in resistivity at low temperatures indicates the effect of the SDW state in the electronic transport. The maximum magnetic-entropy change is $-16.1\,\mathrm{J/kg\,K}$ under a magnetic field change of 0–70 kOe for an isotropic $HoAl_2Ge_2$ powder and it increases to $-17.9\,\mathrm{J/kg\,K}$ for a single crystal when the magnetic field (H) is applied parallel to the *ab* plane. A large rotating magnetic-entropy change of $-5.1\,\mathrm{J/kg\,K}$ for $H = 20\,\mathrm{kOe}$ in a $HoAl_2Ge_2$ single crystal is obtained, which is closely associated to the magnetic anisotropy of the SDW order and its response to the external magnetic field. We discuss the large MCE in terms of the field-induced metamagnetic transition from the incommensurate SDW order to the ferromagnetic order. Our study establishes the triangular lattice RAl_2Ge_2 (R = rare-earth elements) as a unique family of compounds to explore the existence of the incommensurate spin density waves and the correlated physical properties.

DOI: 10.1103/PhysRevB.106.134426

I. INTRODUCTION

The total energy of a spin arrangement in an interacting spin system is usually the sum of the exchange energies for every spin interaction between the nearest neighboring spins, if one neglects the next-nearest neighboring ones. The ground state is determined by minimalizing the total energy, which usually is a collinear spin alignment when only exchange interactions are considered. Therefore, the spin arrangement of a magnetic material tends to be collinear in lots of simple antiferromagnetic (AFM) or ferromagnetic (FM) compounds [1]. However, when there is competition between AFM and FM exchange interactions [including the Ruderman-Kittel-Kasuya-Yosida (RKKY) interaction], or a structure with geometry frustration, or a strong coupling between the spin orbits of electrons, or a magnetic anisotropy affected by a strong crystalline electric field (CEF), etc., the spins may form noncollinearly aligned magnetic superstructures such as cycloid, helix, or spin density wave (SDW) states [2–11]. The SDW is a spin-modulated state in real space, which was first postulated by Overhauser in 1962 to illustrate the AFM ground state of chromium [8]. Besides Cr [12], the SDW was also observed in heavy rare-earth metals [13], and intermetallic compounds CrFe, CuMn, FeAs, etc. [14–16]. The correspondence between the spatial periodicity of the SDW state and the lattice constant can be divided into commensurate or incommensurate SDW. Incommensurate SDW phases originate from either a Fermi surface instability known as nesting from electron-electron interactions, or the coupling of local magnetic moments via the RKKY interaction [8,10,11]. It was reported that the coexistence of magnetic order and metallic conductivity in FeAs-based compounds originated from the incommensurate magnetic ordering in terms of either a SDW or a spiral magnetic structure [16]. Therefore, the incommensurate SDW may induce various unique physical phenomena in magnetic systems.

Recently, large magnetocaloric effect (MCE) and rotating magnetocaloric effect (RMCE) were observed in the $CaAl_2Si_2$-type metallic triangular lattice antiferromagnet $ErAl_2Ge_2$ single crystal [17]. As one of the rare-earth

*shengjm@sustech.edu.cn
†wjren@imr.ac.cn

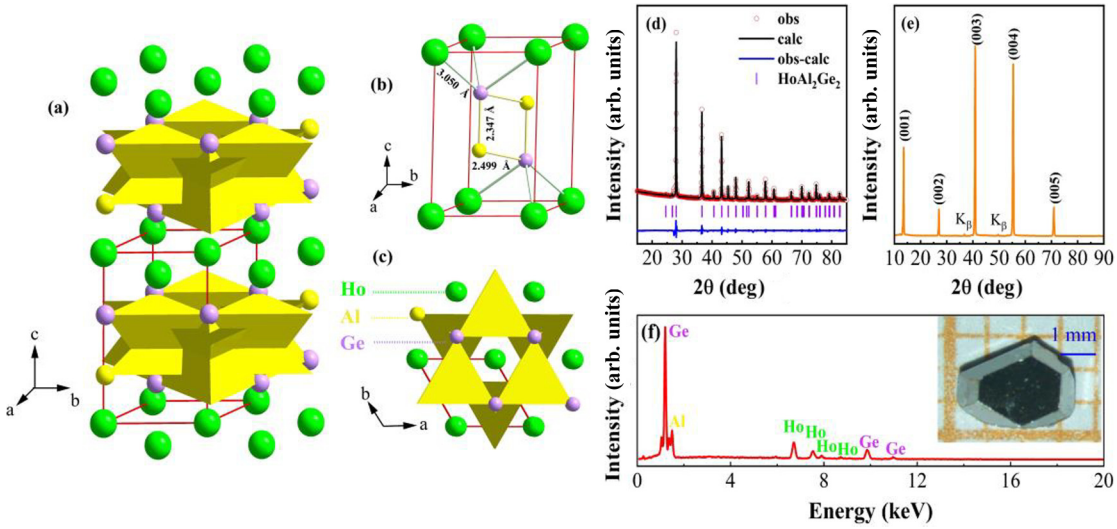

FIG. 1. (a), (c) Polyhedral view crystal structure of $HoAl_2Ge_2$. (b) The unit cell of $HoAl_2Ge_2$. (d) Powder XRD patterns of $HoAl_2Ge_2$ (ground from $HoAl_2Ge_2$ single crystals) and structural refinement results. (e) The XRD pattern of a flat facet of $HoAl_2Ge_2$ single crystal identified to be the (001) plane. (f) The EDX spectroscopy data of the grown crystals; the inset is a photograph of a typical single crystal (the orange square is $1 \times 1\,mm^2$).

RAl_2Ge_2 series compounds, the magnetization curve of $HoAl_2Ge_2$ reveals that it transits from the AFM order to the FM order driven by a very small magnetic field [18]. The magnetization of $HoAl_2Ge_2$ with $6.32\,\mu_B$/Ho in a magnetic field of 20 kOe behaves like a FM compound, which is different from most AFM compounds presenting small magnetization values at low magnetic fields and a linear field dependence up to very high fields. In addition, not much is known yet about the magnetic structures of the rare-earth RAl_2Ge_2 series compounds, and it was conjectured that $ErAl_2Ge_2$ has a canted magnetic structure and the *ab* plane component of the magnetic moments is dominant [19]. Based on the above analysis, $HoAl_2Ge_2$ may exhibit interesting magnetic order and MCE. Therefore, it is particularly interesting to study the physical properties of the metallic triangular lattice $HoAl_2Ge_2$.

In this work, we determine the magnetic structure of the $CaAl_2Si_2$-type metallic triangular lattice $HoAl_2Ge_2$ via neutron powder diffraction (NPD) measurements. Rietveld analysis of the magnetic Bragg pattern is associated with (0.23, 0, 0.06) incommensurate ordering propagation vector, and the relevant basis of magnetic moments reveals that the magnitudes of the magnetic moments are modulated along the crystallographic [1 0 0] and [0 0 1] directions. The magnetic susceptibility $\chi(T)$, magnetization $M(H)$, electrical resistivity $\rho(T)$, heat capacity $C_P(T)$, MCE, and RMCE of the $HoAl_2Ge_2$ single crystal are investigated. The maximum magnetic-entropy change of $-17.9\,J/kg\,K$ under a magnetic field change of 0–70 kOe for the $H \parallel ab$ plane and the rotating magnetic-entropy change of $-5.1\,J/kg\,K$ for $H = 20$ kOe are obtained.

II. EXPERIMENT DETAILS

$HoAl_2Ge_2$ single crystals were prepared by the Al-Ge flux method. High-purity bulk metals Ho, Al, and Ge with a starting atomic composition of 1:30:20 were placed in a high-quality recrystallized-alumina crucible and sealed in an evacuated quartz tube. The ampoule was placed in a furnace and heated to 1323 K at a rate of 100 K/h, kept for 10 h at this temperature to ensure that the original materials were fully mixed and melted, then cooled at a rate of 3 K/h to 873 K. At this temperature, we used centrifugation to remove the excess Al-Ge flux. The obtained single crystals show metallic luster on the surface and have a plateletlike shape with the *c* axis perpendicular to the plane and dimensions of 3 mm × 3 mm × 1 mm. The typical $HoAl_2Ge_2$ single crystal is shown in the inset of Fig. 1(f). The crystal structure and composition are characterized by a Cu $K\alpha$ x-ray diffractometer (XRD, $\lambda = 1.5418$ Å) and a scanning electron microscope (SEM, XL30, Philips). The orientation of the $HoAl_2Ge_2$ single crystal was verified with a Bruker D8 3 kW XRD detector using Cu $K\alpha$ radiation ($\lambda = 1.5418$ Å). The magnetic susceptibility $\chi(T)$ was measured between 2 and 300 K in an applied magnetic field of 100 Oe in the field-cooling (FC) mode using a Quantum Design superconducting quantum interference device (SQUID) magnetometer. Isothermal magnetizations $M(H)$ were measured at 2–28 K in applied magnetic fields up to 70 kOe. The heat capacity $C_P(T)$ and electrical resistivity $\rho(T)$ measurements were carried out in a Quantum Design Physical Property Measurement System (PPMS). The $C_P(T)$ was measured by the thermal relaxation method down to 2 K. The NPD experiments were performed on the time of flight powder diffractometer, POWGEN [20], at the Spallation Neutron Source (SNS), Oak Ridge National Laboratory (ORNL). We gently crushed about 2 g of single crystals into fine powders for NPD experiments. The NPD patterns were collected at 2, 35, and 100 K at POWGEN with the powder loaded in a vanadium container. The obtained NPD patterns were refined by using the Rietveld software package FULLPROF SUITE [21].

III. RESULTS AND DISCUSSION

$HoAl_2Ge_2$ crystallizes in trigonal structure with space group $P\bar{3}m1$ (No. 164), and the rare-earth atom Ho lies in

the 1*a* (0, 0, 0) position with $-3m$ symmetry, whereas Al lies in the 2*d* (1/3, 2/3, 0.63) position and Ge lies in the 2*d* (1/3, 2/3, 0.278) position with 3*m* symmetries, respectively. As illustrated in Fig. 1(a), the Ho atoms form a triangular lattice in the *ab* plane. The Al and Ge atoms form a hexagonal grid and are interspersed between the Ho atomic layers. The nearest neighboring Ho atoms are connected by Ge atoms to form an octahedral structural unit, and the magnetic coupling is realized by the superexchange mechanism of Ho-Ge-Ho. The powder XRD data shown in Fig. 1(d) were collected at 300 K on crushed powders of $HoAl_2Ge_2$ single crystals. Refined results reveal that the crystal is single phase and does not have any impurity phases. The goodness of fit for the trial is the profile factor $R_p = 3.70\%$, the weighted profile factor $R_{wp} = 5.93\%$ and reduced chi square $\chi^2 = 6.85$. The lattice constants obtained are $a = b = 4.191$ Å and $c = 6.672$ Å, in good agreement with the values reported in the literature [18]. From the energy-dispersive x-ray (EDX) spectroscopy data, as represented in Fig. 1(f), the atomic percentages of the $HoAl_2Ge_2$ compound were determined to be Ho, Al, Ge = 19.8, 39.7, 40.5, approaching the perfect stoichiometry 1:2:2. The (0 0 1) plane was identified by XRD on the big flat facet of the $HoAl_2Ge_2$ single crystal, as shown in Fig. 1(e).

Figure 2(a) presents the temperature dependence of the $\chi(T)$ for the magnetic field along the *c* axis and the *ab* plane of a $HoAl_2Ge_2$ crystal, and $\chi(T)$ for a polycrystalline powder sample. The temperature range of the measurement is 2–300 K and the applied magnetic field is 100 Oe. The $\chi(T)$ increases with decreasing the temperature and displays a peak around $T_N = 7$ K, corresponding to the paramagnetic (PM) to AFM transition, which is close to the previously reported ~6.7 K [18]. At low temperatures, the $\chi(T)$ for the $H \parallel ab$ plane of the single crystal is larger than that for the $H \parallel c$ axis. The temperature dependences of the inverse magnetic susceptibility $\chi^{-1} = \frac{H}{M}$ are plotted in Fig. 2(b) and fitted by the modified Curie-Weiss law, $\chi_m = \chi_0 + \frac{C}{T-\theta_P}$, where χ_0 is a temperature independent contribution from the core electrons and the Pauli spin susceptibility of the conduction electrons, *C* is the Curie constant, and θ_P is the Curie-Weiss temperature. For the $H \parallel ab$ plane $\theta_P = -5$ K and for the $H \parallel c$ axis $\theta_P = -12$ K, which suggests weak AFM interactions between the magnetic moments of Ho^{3+}. The effective moment μ_{eff} obtained for the powder sample is 10.19 μ_B per formula unit, which is close to the expected free ion value for a Ho^{3+}.

Figure 2(c) shows the $M(H)$ curves at 2 K for the magnetic field applied along different crystallographic directions and for the powder sample. For all three curves, the $M(H)$ gradually increases with the increase of the magnetic field and shows traces of saturation. From the dM/dH curve in the inset of Fig. 2(c) for the $H \parallel ab$ plane, it can be seen that two obvious discontinuous inflection points exist, which suggests that the magnetic state changes, indicating a field-induced metamagnetic transition from AFM ground state to FM state. This phenomenon can be explained by the modulation of magnetic moments as shown in Fig. 3. At identical magnetic fields, the $M(H)$ for the $H \parallel ab$ plane is clearly larger than that for the $H \parallel c$ axis. Similar characteristics of the magnetization are also found in the isostructural compound $EuAl_2Si_2$ [22] and $ErAl_2Ge_2$ [17,19]. The linear behavior of the $M(H)$ curves

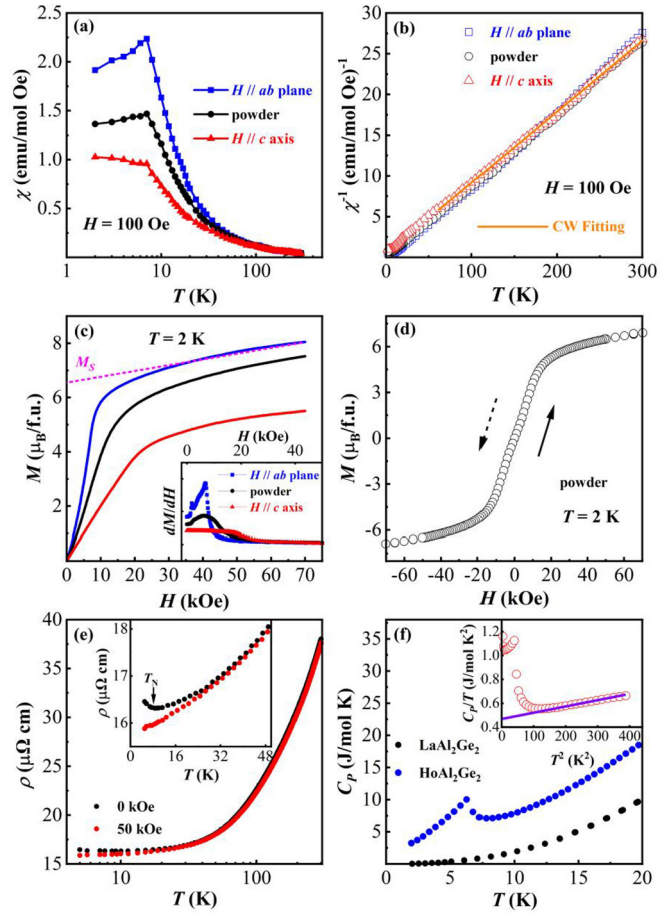

FIG. 2. (a) Temperature dependence of the magnetic susceptibility of $HoAl_2Ge_2$ at a magnetic field of 100 Oe. (b) Temperature dependence of inverse susceptibility χ^{-1} and the fit to the modified Curie-Weiss law. (c) Magnetization versus magnetic field of $HoAl_2Ge_2$ at 2 K. The inset shows the derivatives of isothermal magnetization curves. (d) The magnetization and demagnetization curves at 2 K with the arrows indicating the sweep direction of magnetic field. (e) Temperature dependence of the electrical resistivity measured in zero magnetic field and a magnetic field of 50 kOe along the *c* axis. The inset represents the resistivity in 5–50 K of $HoAl_2Ge_2$. (f) Temperature dependences of the heat capacity of $HoAl_2Ge_2$ and $LaAl_2Ge_2$. The inset displays the relationship curve between C_P/T and T^2 and its fitting curve of $HoAl_2Ge_2$.

observed at high magnetic fields is usually related to the Van Vleck paramagnetism, which is mainly due to the excited CEF effects. A large Van Vleck term is usually observed in rare-earth compounds, such as $PrPt_5$ [23], Eu_2O_3 [24], and $NaYbO_2$ [25], etc. After subtracting the Van Vleck term, it can be seen that the saturation magnetization of the system is approximately 6.32 μ_B/Ho. As depicted in Fig. 2(d), remarkably, the $M(H)$ isotherms were obtained at 2 K for *H* (±70 kOe) showing nonhysteresis characteristics similar to the second-order phase transition materials.

The temperature dependence of $\rho(T)$ of $HoAl_2Ge_2$ was measured from 5 to 300 K by passing a current of 10 mA in the *ab* plane with/without the magnetic field along the *c* axis of the crystal. In Fig. 2(e), the electrical resistivity decreases with decreasing temperature, showing the characteristics of

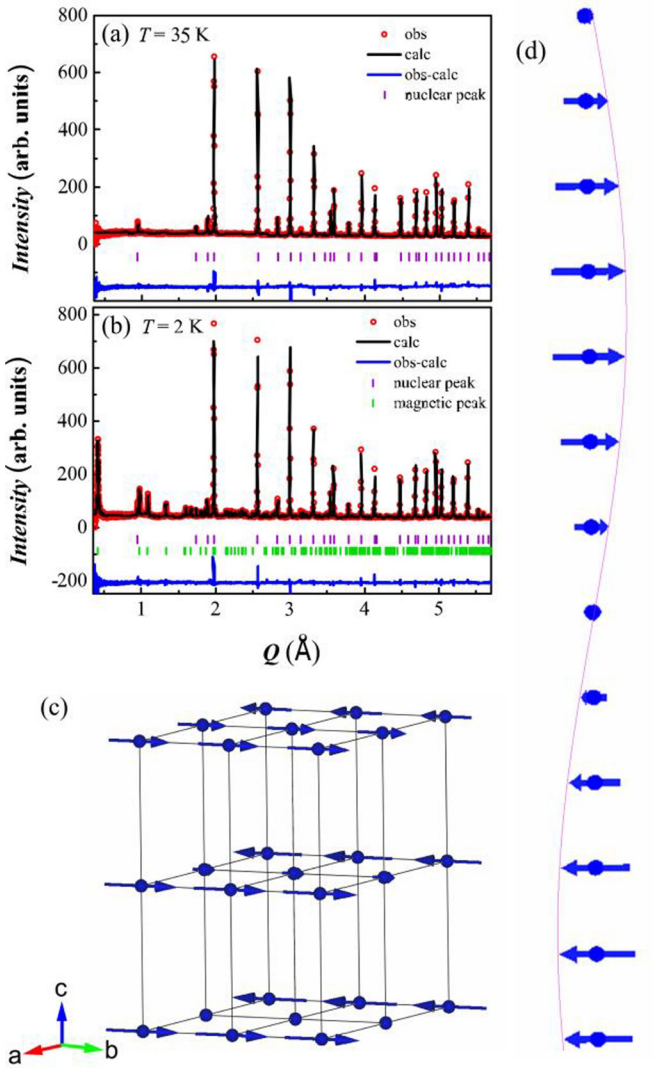

FIG. 3. Rietveld refinement of NPD patterns of $HoAl_2Ge_2$ at (a) 35 K $> T_N$ and (b) 2 K $< T_N$. The experimental data and calculated pattern are shown as open red circles and solid black lines, respectively. The blue lines at the bottom show the difference of the measured and calculated intensities. The violet and green vertical bars indicate the nuclear and magnetic Bragg peaks, respectively. (c) The determined incommensurate magnetic structure of $HoAl_2Ge_2$ with magnetic propagation vector (0.23, 0, 0.06). (d) Magnetic configuration of the incommensurate SDW at 2 K along the c axis.

a metal with the residual resistivity (at 2 K) of 16.5 $\mu\Omega$ cm and a resistivity rising phenomenon appears near T_N due to the SDW transition at low temperatures as will be discussed below. Reference [26] reported that the development of the SDW state leads to the removal of the Fermi surface, which may lead to the increase of the resistivity. This phenomenon was also observed in rare-earth metals such as Dy, Er, Ho, Tm, and in several rare-earth intermetallic compounds [27]. Temperature dependence of the resistivity measured at 50 kOe is similar to that at zero magnetic field, but with smaller values due to the negative magnetoresistance effect, and the minimum resistivity around T_N was smoothed out.

The temperature dependences of the heat capacity of a single crystalline $HoAl_2Ge_2$ and its nonmagnetic reference single crystalline $LaAl_2Ge_2$ in the temperature range 2–20 K are shown in Fig. 2(f). The inset displays the C_P/T-T^2 curve and its fitting. The heat capacity of the magnetic compound $HoAl_2Ge_2$ is greater than that of the nonmagnetic compound $LaAl_2Ge_2$ in the entire temperature range, due to the additional $4f$-derived contribution to the heat capacity C_{4f}. In $HoAl_2Ge_2$, a very sharp λ-shape transition occurs at about 7 K, which is consistent with the AFM transition temperature observed in the magnetic susceptibility measurements shown in Fig. 2(a). C_P/T versus T^2 is linear above T_N fitted by the low-temperature Debye model using the expression of $C_P/T = \gamma + \beta T^2$, where γ is the electronic specific heat coefficient and βT^2 is the low-temperature limit of the lattice term [28]. The fit yields $\gamma = 0.431\,\mathrm{J/mol\,K^2}$, $\beta = 2.488 \times 10^{-5}\,\mathrm{J/mol\,K^4}$ of $HoAl_2Ge_2$, and a value of 303 K for the Debye temperature θ_D is inferred from the lattice heat capacity coefficient β using the relation $\theta_D = \sqrt[3]{12\pi^4 rR/5\beta}$ (where r is the number of atoms in the formula unit). We have estimated the $4f$-derived contribution to the magnetic entropy of $HoAl_2Ge_2$ by integrating the $C_P(T)/T$ data after subtracting the heat capacity of $LaAl_2Ge_2$, assuming the lattice contribution to C_P in $HoAl_2Ge_2$ is identical to $LaAl_2Ge_2$. At $T_N = 7$ K, the magnetic entropy recovers 6.85 J/mol K, which is slightly higher than $R\ln(2)$ and only reaches ∼29% of $R\ln(17)$ expected for the $^5I_8$ ground state of Ho^{3+}.

To determine the magnetic structure of $HoAl_2Ge_2$, NPD experiments were performed at POWGEN. The NPD patterns at 35 K $> T_N$ and 2 K $< T_N$ are illustrated in Figs. 3(a) and 3(b), respectively. The structural Rietveld refinement at 35 K confirms the trigonal structure of $HoAl_2Ge_2$ with space group $P\bar{3}m1$. This is consistent with XRD results at room temperature and also indicates there is no extra structural transition with lowering temperature. At $T = 2$ K, besides the nuclear Bragg reflections, an additional set of reflections due to the magnetic order of the Ho^{3+} moments emerges in the diffraction pattern [shown by the green bars in Fig. 3(b)]. By using the K-SEARCH program included with FULLPROF SUITE [21], we found all the magnetic reflections could be indexed by the propagation vector $\boldsymbol{k} = (0.23, 0, 0.06)$. However, in isostructural $EuAl_2Si_2$, it was reported that Eu^{3+} $4f$ moments are collinear AFM structure made up by alternating/stacking of FM layers parallel to the (001) plane with a wave vector $\boldsymbol{k} = (0, 0, 0.5)$ [29]. Next, representation analysis was applied to analyze the possible magnetic structures [30]. For the space group $P\bar{3}m1$ with a Ho^{3+} site at (0,0,0) and $\boldsymbol{k} = (0.23, 0, 0.06)$, the magnetic configuration can be determined by two different irreducible representations (IRs). For IRs Γ_1, it constrains the moments lying in the ab plane, while for IRs Γ_2, it allows the moments mainly along the c axis. By Rietveld refinement, we found IRs Γ_1 can be best fitted with the magnetic diffraction pattern at 2 K with $R_p = 4.95\%$, $R_{wp} = 5.00\%$, and $\chi^2 = 13.60$. The determined magnetic structure of $HoAl_2Ge_2$ is illustrated in Fig. 3(c). $HoAl_2Ge_2$ has an incommensurate magnetic structure; the moments of Ho^{3+} are modulated by $k_x = 0.23$ and $k_z = 0.06$ along the [100] and [001] directions, respectively. The moments point to the a or b axis. Here, we show the moment

direction pointing along the b axis in Fig. 3(c). The determined ordered moment of Ho^{3+} is about 6.22(5) μ_B/Ho, which is consistent with the saturation moment ($M_S = 6.32\,\mu_B$) derived from the magnetization curves at 2 K in Fig. 2(b). The magnetic moment value obtained by NPD is slightly smaller than the saturation moment of Ho^{3+}, which also appears in HoAlGa [31] and $HoAgSb_2$ [32]. The relatively small magnetic moment is in agreement with a SDW in the weak-coupling limit [26]. We can clearly see that the magnetic moments are arranged along the c axis in the form of a SDW in Fig. 3(d). Note that the SDW order has a special propagation vector (0.23, 0, 0.06), indicative of a modulation of spin order/moment along both the in-plane a and out of plane c directions. As compared to other rare-earth based compounds, this type of SDW order is unusual. The modulated magnetic arrangements have also been found in HoAlGa, DyAlGa, $R(Al_xGa_{1-x})_2$, $DyGa_2$, and $HoGa_2$, etc. [31,33–36]. Between $T_t = 18.5$ K and $T_N = 31$ K, HoAlGa has a sine wave modulated structure with an incommensurate propagation vector $\boldsymbol{k} = (1/3, 1/3, 0.481)$; unlike $HoAl_2Ge_2$, the moment is only modulated along the c axis in HoAlGa. Different from HoAlGa, DyAlGa has a sine wave structure of a propagation vector $\boldsymbol{k} = (1/3, 1/3, 1/2)$ between $T_t = 20$ K and $T_N = 50$ K with Dy moments along the c axis and shows a progressive squaring magnetic structure at lower temperature. $HoGa_2$ has a mixing of a simple collinear AFM structure with $\boldsymbol{k} = (0, 1, 0)$ and an incommensurate amplitude-modulated structure of $\boldsymbol{k} = (0.123, 1, 0)$ with the moment along both a and b axes for 6.5 K $< T <$ 7.6 K. $DyGa_2$ has a collinear modulated structure for 11 K $> T >$ 6.1 K with $\boldsymbol{k} = (0.134, 1, 0)$, 1, 0) and a simple AFM structure with $\boldsymbol{k} = (0, 1, 0)$ below 6.1 K. They are interesting because their uniaxial anisotropy leads to Ising-like or to XY-like magnetic moment systems, and the exchange interaction Hamiltonian can often be reduced to a pseudo-two-dimensional lattice. In particular, these compounds give an excellent example of the different magnetic arrangements which can be stabilized in a two-dimensional triangular lattice in both Ising-like and XY-like systems.

Rare-earth intermetallic compounds easily form modulated magnetic structures such as the SDW, and this result helps us to understand the origin of large MCE in antiferromagnet $HoAl_2Ge_2$. In order to study the MCE of $HoAl_2Ge_2$, we measured the magnetic isotherm curves of $HoAl_2Ge_2$ as shown in Fig. 4(a) for the $H \parallel ab$ plane, Fig. 4(b) for the $H \parallel c$ axis, and Fig. 4(c) for powder in the temperature range 2–28 K with temperature steps of 2 K. The magnetization generally decreases with the increase of temperature. At the identical temperature, the magnetization for a single crystal with the $H \parallel ab$ plane is larger than that for the single crystal with the $H \parallel c$ axis, while that for powder is in between because of the averaging effect. Figure 4(d) represents magnetic isotherm curves of $HoAl_2Ge_2$ for powder in the temperature range 2–60 K. We can see that with the temperature increases, $M(H)$ gradually tends to be linear. The $M(H)$ becomes completely linear until the temperature rises to 40 K, which indicates that there is a short-range correlation above T_N.

Because there is no magnetic hysteresis in the $M(H)$ curves, this material may be a good magnetic refrigeration material. The magnetic-entropy change ΔS_M was derived by

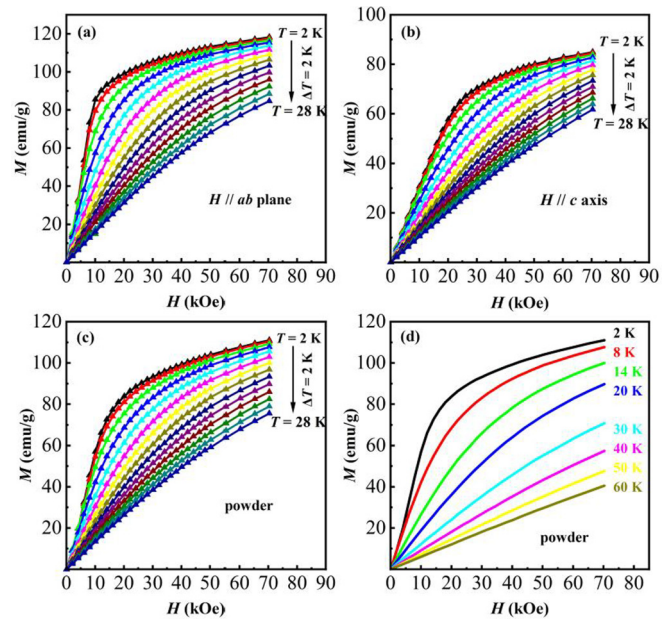

FIG. 4. Magnetic isotherm curves of $HoAl_2Ge_2$ (a) for the $H \parallel ab$ plane, (b) for the $H \parallel c$ axis, and (c) for powder in the temperature range 2–28 K with temperature steps of 2 K, and (d) for powder in the temperature range 2–60 K.

means of the Maxwell equation:

$$\Delta S_M(T,\ \Delta H) = S_M(T,\ H) - S_M(T,\ 0) = \int_0^H \left(\frac{\partial S}{\partial H}\right)_T = \int_0^H \left(\frac{\partial M}{\partial T}\right)_H dH. \quad (1)$$

Figures 5(a)–5(c) present the magnetic-entropy change with the temperature of a $HoAl_2Ge_2$ single crystal and of a powder sample. It can be seen that ΔS_M exhibits a broad hump around T_N with negative values. At 11 K and for a magnetic field change from 0 to 70 kOe, the maximum magnetic-entropy change of the polycrystalline powder sample is -16.1 J/kg K. The maximum magnetic-entropy changes for the magnetic field along the ab plane and the c axis are -17.9 and -11.6 J/kg K, respectively. Compared with the other reported MCE materials, $HoAl_2Ge_2$ single crystals have superior MCE performance compared to some other MCE materials, such as $TmFeO_3$ [37], RMn_2O_5 (R = Tb and Ho) [38,39], $RMnO_3$ (R = Ho, Yb, Dy, and Tm) [40–42], Tb_2CoMnO_6 [43], and $HoNiGe_3$ [44]. Strictly speaking, the magnitude of the magnetic-entropy change is typical, but unlike other MCE materials, the large magnetic-entropy change in $HoAl_2Ge_2$ originates from the field-induced metamagnetic transition from incommensurate SDW order to FM order, and the magnetic anisotropy plays an important role in the MCE. The maximum value for the $H \parallel ab$ plane is 11% larger than that for the polycrystalline sample. The maximum magnetic-entropy change of the single crystal with the $H \parallel ab$ plane is much larger than the single crystal with the $H \parallel c$ axis and powder sample. This result is consistent with the fact that the magnetic moments tend to be more aligned in the ab plane. It shows that the magnetic materials with strong anisotropy

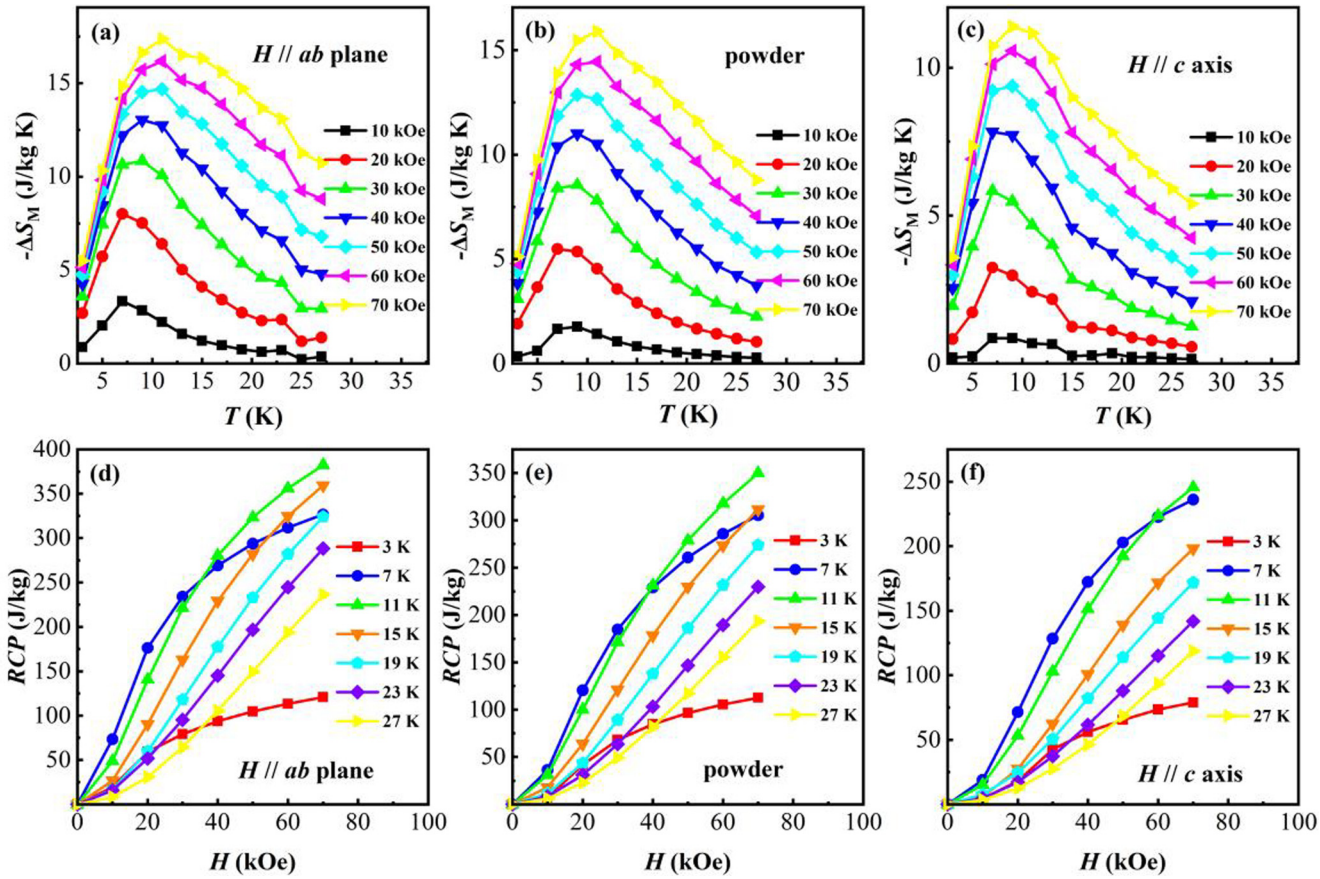

FIG. 5. (a) Magnetic-entropy change of $HoAl_2Ge_2$ versus temperature (a) for the $H \parallel ab$ plane, (b) for powder and (c) for the $H \parallel c$ axis. Magnetic field dependence of *RCP* of $HoAl_2Ge_2$ for (d) the $H \parallel ab$ plane, (e) for powder, and (f) for the $H \parallel c$ axis at different temperatures.

have better MCE performance than polycrystalline samples. The adiabatic temperature change (ΔT_{ad}) can be evaluated by means of the following equation:

$$\Delta T_{ad}(T,\ \Delta H) \approx -\frac{T}{C_P}\Delta S_M(T,\ \Delta H). \tag{2}$$

The maximum adiabatic temperature changes for the $H \parallel ab$ plane are about 3 and 9 K for magnetic field changes of 0–20 and 0–70 kOe, respectively, by using the specific heats $C_P(7\,\mathrm{K}) = 7.24\,\mathrm{J/mol\,K}$ and $C_P(11\,\mathrm{K}) = 8.03\,\mathrm{J/mol\,K}$ corresponding to the maximum magnetic-entropy change of $HoAl_2Ge_2$ in Fig. 2(f).

The relative cooling power (RCP) can be calculated by the following equation,

$$\mathrm{RCP} = |\Delta S_{\max}|\delta T, \tag{3}$$

where $\Delta S_{\max}$ is the maximum magnetic-entropy change and δT is the full width at half maximum of the $\Delta S_M(T)$ curve. Figures 5(d)–5(f) show the magnetic field dependence of RCP for the $H \parallel ab$ plane, for the powder sample, and for the $H \parallel c$ axis. For a magnetic field change of 0–70 kOe, the RCP values for the $H \parallel ab$ plane, for powder, and for the $H \parallel c$ axis are 383, 350, and 251 J/kg, respectively.

We can use the magnetic anisotropy of a single crystal to obtain the rotating magnetic-entropy change by rotating the magnetic field along the directions of the crystal. The rotating magnetic-entropy change ΔS_R obtained by rotating the magnetic field along the c axis to the ab plane can be represented as follows:

$$\begin{aligned}
&\Delta S_R(T,\ H,\ c \to ab)\\
&= S_M^{H\parallel ab}(T,\ H) - S_M^{H\parallel c}(T,\ H)\\
&= \left[S_M^{H\parallel ab}(T,\ H) - S_M(T,\ 0)\right]\\
&\quad -\left[S_M^{H\parallel c}(T,\ H) - S_M(T,\ 0)\right]\\
&= S_M^{H\parallel ab}(T,\ \Delta H) - S_M^{H\parallel c}(T,\ \Delta H).
\end{aligned} \tag{4}$$

The above formula can be expressed by the following formula:

$$\begin{aligned}
&\Delta S_R(T,\ H,\ c \to ab)\\
&= \int_0^H \left(\frac{\partial M_{ab}}{\partial T}\right)dH - \int_0^H \left(\frac{\partial M_c}{\partial T}\right)dH\\
&= \int_0^H \left(\frac{\partial (M_{ab} - M_c)}{\partial T}\right)dH.
\end{aligned} \tag{5}$$

M_{ab} and M_c are the magnetization values when the magnetic field is along the ab plane and c axis, respectively. Figure 6(a) gives the rotating magnetic-entropy change as a function of magnetic field and temperature. With increasing temperature, the rotating magnetic-entropy change gradually increases, and the maximum value is $-5.1\,\mathrm{J/kg\,K}$ at 9 K for

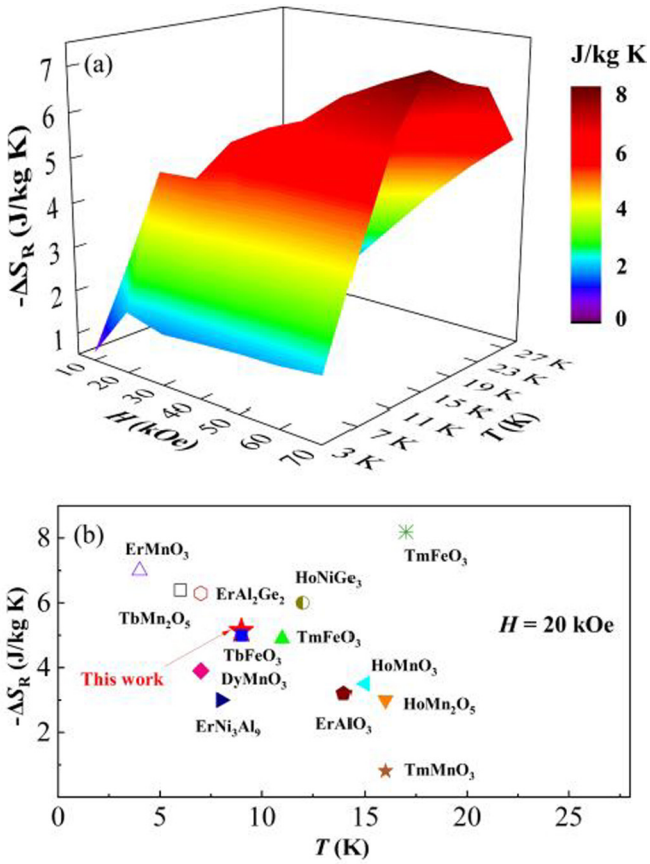

FIG. 6. (a) Rotating magnetic-entropy change as a function of magnetic field and temperature. (b) The rotating magnetic-entropy change for $HoAl_2Ge_2$ single crystal in comparison with other reported RMCE materials under constant fields of 20 kOe [17,37–42,44–47].

$H = 20$ kOe. Compared with other RMCE materials reported previously, as shown in Fig. 6(b), $HoAl_2Ge_2$ single crystal is comparable to some RMCE materials at 20 kOe. Note that the origin of the RMCE in $HoAl_2Ge_2$ is closely associated with the strong magnetic anisotropy of the unusual SDW order and its response to the external magnetic field. A particularly interesting aspect of $HoAl_2Ge_2$ is the maximum rotating adiabatic temperature change ($\Delta T_{ad,ca}$) of 3.2 K at $H = 20$ kOe, which is larger than that of $HoMn_2O_5$ [39] and $ErMnO_3$ [45] single crystals under 20 kOe.

IV. CONCLUSION

To summarize, we report the incommensurate spin density waves, and the resultant anisotropic and rotating magnetocaloric properties in $HoAl_2Ge_2$. In $T < T_N$, it exhibits an incommensurate structure modulated by the propagation vector of (0.23, 0, 0.06) with a moment size of 6.22(5) μ_B/Ho. The response of the incommensurate SDW in $HoAl_2Ge_2$ induces a large anisotropic and RMCE in the liquid helium temperature region. For a magnetic field change of 0–70 kOe at 11 K, $\Delta S_M = -11.6$ J/kg K for a single crystal with the $H \parallel c$ axis and -17.9 J/kg K for a single crystal with the $H \parallel ab$ plane. When $H = 20$ kOe, a large rotating magnetic-entropy change of -5.1 J/kg K can be obtained by using the magnetic anisotropy of the $HoAl_2Ge_2$ single crystal. Further inelastic neutron scattering experiments at zero magnetic field and high magnetic fields are required to unveil the magnetic interactions for deep understanding of the appearance of the incommensurate SDW and the large MCE in $HoAl_2Ge_2$.

ACKNOWLEDGMENTS

This work has been supported by the Ministry of Science and Technology of China (Grants No. 2020YFA0406002 and No. 2021YFB3501201) and the National Natural Science Foundation of China (Grants No. 52071323, No. 12104255, No. 52031014, and No. 12134020). A portion of this research used resources at the Spallation Neutron Source, a DOE Office of Science User Facility operated by the Oak Ridge National Laboratory.

[1] H.-J. Koo, R. R. P N, F. Orlandi, A. Sundaresan, and M.-H. Whangbo, On ferro- and antiferro-spin-density waves describing the incommensurate magnetic structure of $NaYNiWO_6$, Inorg. Chem. **59**, 17856 (2020).

[2] H. J. Xiang, S.-H. Wei, M.-H. Whangbo, and J. L. F. Da Sliva, Spin-Orbit Coupling and Ion Displacements in Multiferroic $TbMnO_3$, Phys. Rev. Lett. **101**, 037209 (2008).

[3] E. J. Kan, H. J. Xiang, Y. Zhang, C. Lee, and M.-H. Whangbo, Density-functional analysis of spin exchange and ferroelectric polarization in $AgCrO_2$, Phys. Rev. B **80**, 104417 (2009).

[4] C. H. Lee, E. Kan, H. J. Xiang, and M.-H. Whangbo, Theoretical investigation of the magnetic structure and ferroelectric polarization of the multiferroic langasite $Ba_3NbFe_3Si_2O_{14}$, Chem. Mater. **22**, 5290 (2010).

[5] X. Z. Lu, M.-H. Whangbo, S. Dong, X. G. Gong, and H. J. Xiang, Giant Ferroelectric Polarization of $CaMn_7O_{12}$ Induced by a Combined Effect of Dzyaloshinskii-Moriya Interaction and Exchange Striction, Phys. Rev. Lett. **108**, 187204 (2012).

[6] J. H. Yang, Z. L. Li, X. Z. Lu, M.-H. Whangbo, S.-H. Wei, X. G. Gong, and H. J. Xiang, Strong Dzyaloshinskii-Moriya Interaction and Origin of Ferroelectricity in Cu_2OSeO_3, Phys. Rev. Lett. **109**, 107203 (2012).

[7] H. J. Xiang, C. H. Lee, H.-J. Koo, X. G. Gong, and M.-H. Whangbo, Magnetic properties and energy-mapping analysis, Dalton Trans. **42**, 823 (2013).

[8] A. W. Overhauser, Spin density waves in an electron gas, Phys. Rev. **128**, 1437 (1962).

[9] G. Gruner, *Density Waves in Solids* (Academic, San Diego, CA, 1994).

[10] A. W. Overhauser, Structure of Nuclear Matter, Phys. Rev. Lett. **4**, 226 (1960).

[11] Y. Wu, Z. H. Ning, H. B. Cao, G. X. Cao, K. A. Benavides, S. Karna, G. T. McCandless, R. Jin, J. Y. Chan, W. A. Shelton, and J. F. DiTusa, Spin density wave instability in a ferromagnet, Sci. Rep. **8**, 5225 (2018).

[12] E. Fawcett, Spin-density-wave antiferromagnetism in chromium, Rev. Mod. Phys. **60**, 209 (1988).

[13] R. J. Elliott and F. A. Wedgwood, The temperature dependence of magnetic ordering in the heavy rare earth metals, Proc. Phys. Soc., London **84**, 63 (1964).

[14] Y. Tsunoda, The commensurate-incommensurate SDW phase boundary of CrFe alloys, J. Phys.: Condens. Matter. **6**, 8513 (1994).

[15] J. A. Gotaas, J. J. Rhyne, and S. A. Werner, Spin density waves in Cu-Mn, J. Appl. Phys. **57**, 3404 (1985).

[16] E. E. Rodriguez, C. Stock, K. L. Krycka, C. F. Majkrzak, P. Zajdel, K. Kirshenbaum, N. P. Butch, S. R. Saha, J. Paglione, and M. A. Green, Noncollinear spin-density-wave antiferromagnetism in FeAs, Phys. Rev. B **83**, 134438 (2011).

[17] F. Gao, W. J. Ren, Y. X. Zhuang, X. G. Zhao, B. Li, and Z. D. Zhang, Magnetocaloric effect of an antiferromagnetic $ErAl_2Ge_2$ single crystal, J. Magn. Magn. Mater. **533**, 168014 (2021).

[18] M. Matin, R. Mondal, A. Thamizhavel, A. Provino, P. Manfrinetti, and S. K. Dhar, Single crystal growth and anisotropic magnetic properties of $HoAl_2Ge_2$, AIP Adv. **8**, 055709 (2018).

[19] M. Nandi, A. Thamizhavel, and S. K. Dhar, Anisotropic magnetic properties of trigonal $ErAl_2Ge_2$ single crystal, J. Phys: Condens. Matter **32**, 185803 (2020).

[20] H. Fuess, P. Scardi, and U. Welzel (eds.), *Proceedings of the Twelfth European Powder Diffraction Conference, August 2010, Darmstadt, Germany* (Oldenbourg Wissenschaftsverlag, München, 2015).

[21] J. Rodríguez-Carvajal, Recent advances in magnetic structure determination by neutron powder diffraction, Physica B (Amsterdam) **192**, 55 (1993).

[22] A. Maurya, R. Kulkarni, A. Thamizhavel, P. Bonville, and S. K. Dhar, Anisotropic magnetic properties of $EuAl_2Si_2$, J. Phys: Conf. Ser. **592**, 012045 (2015).

[23] K. Andres and E. Bucher, Hyperfine enhanced nuclear magnetic cooling in Van Vleck paramagnetic intermetallic compounds, J. Appl. Phys. **42**, 1522 (1971).

[24] H. Samata, N. Wada, and T. C. Ozawa, Van Vleck paramagnetism of europium oxyhydroxide, J. Rare Earths **33**, 177 (2015).

[25] J. Guo, X. G. Zhao, S. Ohira-Kawamura, L. S. Ling, L. H. He, K. J. Nakajima, B. Li, and Z. D. Zhang, Magnetic-field and composition tuned antiferromagnetic instability in the quantum spin-liquid candidate $NaYbO_2$, Phys. Rev. Mater. **4**, 064410 (2020).

[26] G. Grüner, The dynamics of spin-density waves, Rev. Mod. Phys. **66**, 1 (1994).

[27] R. Elliott and F. Wedgwood, Theory of the resistance of the rare earth metals, Proc. Phys. Soc. **81**, 846 (1963).

[28] K. W. Chen, Y. Lai, Y. C. Chiu, S. Steven, T. Besara, D. Graf, T. Siegrist, T. E. Albrecht-Schmitt, L. Balicas, and R. E. Baumbach, Possible devil's staircase in the Kondo lattice CeSbSe, Phys. Rev. B **96**, 014421 (2017).

[29] P. Schobinger-Papamantellos and F. Hulliger, The magnetic structure of $EuAl_2Si_2$, J. Less-Common Met. **146**, 327 (1989).

[30] E. F. Bertaut, Representation analysis of magnetic structures, Acta Crystallogr., Sect. A **24**, 217 (1968).

[31] A. R. Ball, D. Gignoux, D. Schmitt, and F. Y. Zhang, Quantitative analysis of the complex magnetic phase diagram of HoAlGa, Phys. Rev. B **47**, 11887 (1993).

[32] G. André, F. Bouré, M. Kolenda, B. Leśniewska, A. Oleś, and A. Szytuła, Magnetic structures of $RAgSb_2$ compounds, Physica B (Amsterdam) **292**, 176 (2000).

[33] D. Gignoux, D. Schmitt, J. Voiron, F. Y. Zhang, E. Bauer, and G. Schaudy, Magnetic phase diagram of the hexagonal DyAlGa compound, J. Alloys Compd. **191**, 139 (1993).

[34] D. Gignoux, D. Schmitt, A. Takeuchi, and F. Y. Zhang, C. Rouchon, and E. Roudaut, Magnetic properties and structures of the hexagonal HoAlGa compound, J. Magn. Magn. Mater. **98**, 333 (1991).

[35] D. Gignoux, D. Schmitt, and F. Y. Zhang, Magnetic incommensurability in hexagonal $HoGa_2$, J. Alloys Compd. **234**, 239 (1996).

[36] D. Gignoux, D. Schmitt, A. Takeuchi, and F. Y. Zhang, Complex magnetic phase diagram in the hexagonal $DyGa_2$ compound, J. Magn. Magn. Mater. **97**, 15 (1991).

[37] Y. J. Ke, X. Q. Zhang, Y. Ma, and Z. H. Cheng, Anisotropic magnetic entropy change in $RFeO_3$ single crystals (R = Tb, Tm, or Y), Sci. Rep. **6**, 19775 (2016).

[38] M. Balli, S. Jandl, P. Fournier, and D. Z. Dimitrov, Giant rotating magnetocaloric effect at low magnetic fields in multiferroic $TbMn_2O_5$ single crystals, Appl. Phys. Lett. **108**, 102401 (2016).

[39] M. Balli, S. Jandl, P. Fournier, and M. M. Gospodinov, Anisotropy-enhanced giant reversible rotating magnetocaloric effect in $HoMn_2O_5$ single crystal, Appl. Phys. Lett. **104**, 232402 (2014).

[40] M. Balli, S. Mansouri, S. Jandl, P. Fournier, and D. Z. Dimitrov, Large rotating magnetocaloric effect in the orthorhombic $DyMnO_3$ single crystal, Solid State Commun. **239**, 9 (2016).

[41] W. Wang, Y. Li, L. Y. Li, Q. J. Li, D. D. Wang, J. Y. Zhu, J. Li, and M. Zeng, The observed topological vortex domains and the rotating magnetocaloric effect in the hexagonal $RMnO_3$ (R = Ho, Er, and Yb) crystals, J. Phys.: Condens. Matter. **33**, 015802 (2021).

[42] J. L. Jin, X. Q. Zhang, H. Ge, and Z. H. Cheng, Rotating field entropy change in hexagonal $TmMnO_3$ single crystal with anisotropic paramagnetic response, Phys. Rev. B **85**, 214426 (2012).

[43] J. Y. Moon, M. K. Kim, D. G. Oh, J. H. Kim, H. J. Shin, Y. J. Choi, and N. Lee, Anisotropic magnetic properties and giant rotating magnetocaloric effect in double-perovskite Tb_2CoMnO_6, Phys. Rev. B **98**, 174424 (2018).

[44] X. W. Zhao, X. M. Zheng, J. Qi, X. H. Luo, S. C. Ma, S. U. Rehman, W. J. Ren, C. C. Chen, and Z. C. Zhong, Anisotropic magnetocaloric effect and magnetoresistance in antiferromagnetic $HoNiGe_3$ single crystal, Intermetallics **138**, 107307 (2021).

[45] M. Balli, S. Jandl, P. Fournier, J. Vermette, and D. Z. Dimitrov, Unusual rotating magnetocaloric effect in the hexagonal $ErMnO_3$ single crystal, Phys. Rev. B **98**, 184414 (2018).

[46] X. W. Zhao, X. M. Zheng, X. H. Luo, S. C. Ma, Z. S. Zhang, K. Liu, J. Qi, H. Zeng, S. U. Rehman, W. J. Ren, C. C. Chen, and Z. C. Zhong, Giant rotating magnetocaloric effect enhanced by crystal electric field in antiferromagnetic $ErNi_3Al_9$ single crystal, J. Alloys Compd. **847**, 156478 (2020).

[47] X. Q. Zhang, Y. D. Wu, Y. Ma, Q. Y. Dong, Y. J. Ke, and Z. H. Cheng, Large rotating magnetocaloric effect in $ErAlO_3$ single crystal, AIP Adv. **7**, 056418 (2017).